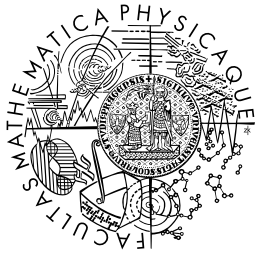

FACULTY
OF MATHEMATICS
AND PHYSICS
Charles University

Summary of doctoral thesis

Jiří Vackář

Automated determination of earthquake source parameters

Department of Geophysics

Supervisor of the doctoral thesis:	prof. RNDr. Jiří Zahradník, DrSc.
Study programme:	physics
Study branch:	geophysics

Prague 2018

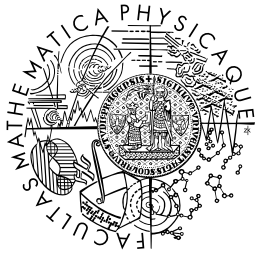

MATEMATICKO-FYZIKÁLNÍ
FAKULTA
Univerzita Karlova

Autoreferát dizertační práce

Jiří Vackář

Automatizace určování zdrojových parametrů zemětřesení

Katedra geofyziky

Vedoucí disertační práce:	prof. RNDr. Jiří Zahradník, DrSc.
Studijní program:	Fyzika
Studijní obor:	Geofyzika

Praha 2018

Dizertace byla vypracována na základě výsledků získaných v letech 2012–2018 během doktorandského studia na Katedre geofyziky MFF UK a v rámci projektu SCIEX na ETH v Curychu.

Dizertant:
Jiří Vackář

Školitel:
prof. RNDr. Jiří Zahradník, DrSc.
Katedra geofyziky MFF UK
V Holešovičkách 2, 180 00 Praha 8

Oponenti:
Prof. RNDr. Tomáš Fischer, Ph.D.
Přírodovědecká fakulta Univerzity Karlovy
Albertov 6, Praha 2

Dr. Christos P. Evangelidis
National Observatory of Athens
Atény, Řecko

Předsedkyně oborové rady:
Doc. RNDr. Hana Čížková, Ph.D.
Katedra geofyziky MFF UK
V Holešovičkách 2, 180 00 Praha 8

Obhajoba dizertace se koná dne 21. 9. 2018 od 10.00 hodin před komisí pro obhajoby dizertačních prací v oboru Geofyzika v budově MFF UK, Ke Karlovu 3, Praha 2 v místnosti M252.

S dizertací je možno se seznámit v PGS MFF UK, Ke Karlovu 3, Praha 2.

Contents

Introduction

The thesis deals with methods for automated inversion of seismic source parameters. We studied the influence of structure model used and show an example how the existing model can be improved. We have developed a new, fully automated tool for the centroid moment tensor (CMT) inversion in a Bayesian framework. It includes automated data retrieval from ArcLink server or local data storage. Step-like disturbances are detected using modeling of the disturbance according to instrument parameters and such components are automatically excluded from further processing. Frequency ranges for the filtration and time windows for the inversion are determined automatically due to epicentral distance. Full-waveform inversion is performed in a space-time grid around a provided hypocenter. A data covariance matrix calculated from pre-event noise yields an automated weighting of the station recordings according to their noise levels and also serves as an automated frequency filter suppressing noisy frequency ranges. The method is tested on synthetic and observed data. It is applied on a dataset from the Swiss seismic network and the results are compared with the existing high-quality MT catalog. The software package programmed in Python is designed to be as versatile as possible in order to be applicable in various networks ranging from local to regional. The method can be applied either to the everyday network data flow, or to process large pre-existing earthquake catalogues and data sets.

1 Bayesian formulation of the inverse problem of centroid moment tensor

A Bayesian approach is a probabilistic method projecting data errors and prior information into the uncertainty of model parameters. In addition to the best-fitting CMT solution, the method provides a posterior probability density function (PPDF) of the parameters. The PPDF can be obtained analytically for linear inverse problems in a L^2-norm and Gaussian distributions of data uncertainties. For non-linear problems a systematic grid search can be used, but (except for problems with very few parameters) it is computationally highly inefficient. That is why stochastic sampling algorithms have been developed to provide an approximation of the PPDF [Sambridge, 2014; Sambridge and Mosegaard, 2002].

Here we propose a hybrid approach, where the centroid position and time are evaluated on a grid of points, and the MT is solved by least squares. In each grid point the PPDF of the MT solution (which is Gaussian because the problem is linear) is obtained analytically. Then such PPDFs are combined to obtain a full (non-Gaussian) PPDF. So we obtain the same PPDF as would be obtained by a stochastic method, but using just a 4-dimensional grid search instead of sampling a 10-dimensional model space. The grid is chosen in such a way that it covers all relevant locations and its sampling density controls PPDF discretization. By choosing the grid, we define a prior information for centroid location and time, which is uniform within the grid and zero elsewhere. In other words, we assume that the hypocenter definitely lies within the grid, but no position within the grid is preferred.

In the linear MT problem in a given space-time grid point i (x_i, y_i, z_i, t_i) the observables $\boldsymbol{d}$ and model parameters $\boldsymbol{m}$ are related by $\boldsymbol{d} = \mathbf{G}\boldsymbol{m}$, where matrix $\mathbf{G}$ (forward problem matrix) is composed of Green's functions (more exactly, the forward problem matrix $\mathbf{G}$ in our method is composed of elementary seismograms of 6 elementary moment tensors, which are calculated from Green's functions). Let the measured data, which include measurement uncertainties, be denoted $\boldsymbol{d}_{obs}$, and assume that their uncertainties are Gaussian with the data covariance matrix denoted as $\mathbf{C}_D$ (the content of the data covariance matrix is described in the next Chapter 3). With no prior information about the MT parameters (i.e., formally, Gaussian prior with infinite variance), the least-squares solution for the model parameters is [Tarantola, 2005, eq. 3.40–3.41]

$$\widetilde{\boldsymbol{m}}_i = \left(\mathbf{G}_i^T \mathbf{C}_D^{-1} \mathbf{G}_i\right)^{-1} \mathbf{G}_i^T \mathbf{C}_D^{-1} \boldsymbol{d}_{obs} \ , \tag{1}$$

where $\widetilde{\boldsymbol{m}}_i$ denotes the inverted model parameters in grid point i, which generally differ from the true model parameters $\boldsymbol{m}$. The uncertainties of the model parameters are described by the model parameters covariance matrix $\widetilde{\mathbf{C}}_i^M$, given by

$$\widetilde{\mathbf{C}}_i^M = \left(\mathbf{G}_i^T \mathbf{C}_D^{-1} \mathbf{G}_i\right)^{-1} \ . \tag{2}$$

The misfit value is then

$$\text{misfit}_i = \left(\boldsymbol{d}_{obs} - \mathbf{G}_i \widetilde{\boldsymbol{m}}_i\right)^T \mathbf{C}_D^{-1} \left(\boldsymbol{d}_{obs} - \mathbf{G}_i \widetilde{\boldsymbol{m}}_i\right) \ . \tag{3}$$

The PPDF for MT components in a fixed space-time point i is given by 6-dimensional Gaussian function which is centered in the best solution for the given

grid point i,

$$\mathrm{PPDF}_i(\boldsymbol{m}) = \frac{1}{c} \exp\left(-\frac{1}{2} \left(\boldsymbol{d}_{obs} - \mathbf{G}_i \boldsymbol{m}\right)^T \mathbf{C}_D^{-1} \left(\boldsymbol{d}_{obs} - \mathbf{G}_i \boldsymbol{m}\right)\right) , \tag{4}$$

where c is a constant normalizing the total (10-dimensional) PPDF to unity (see lower). After an algebra, the PPDF can be equivalently written

$$\begin{aligned}
&\mathrm{PPDF}_i(\boldsymbol{m}) = \\
&= \frac{1}{c} \exp\left(-\frac{1}{2} \left[\left(\boldsymbol{d}_{obs} - \mathbf{G}_i \boldsymbol{m}\right)^T \mathbf{C}_D^{-1} \left(\boldsymbol{d}_{obs} - \mathbf{G}_i \boldsymbol{m}\right)\right]\right) = \\
&= \frac{1}{c} \exp\left(-\frac{1}{2} \left[\left(\boldsymbol{m} - \widetilde{\boldsymbol{m}}_i\right)^T \tilde{\mathbf{C}}_M^{-1} \left(\boldsymbol{m} - \widetilde{\boldsymbol{m}}_i\right) + \left(\boldsymbol{d}_{obs} - \mathbf{G}_i \widetilde{\boldsymbol{m}}_i\right)^T \mathbf{C}_D^{-1} \left(\boldsymbol{d}_{obs} - \mathbf{G}_i \widetilde{\boldsymbol{m}}_i\right)\right]\right) = \\
&= \frac{1}{c} \exp\left(-\frac{1}{2} \left[\left(\boldsymbol{m} - \widetilde{\boldsymbol{m}}_i\right)^T \tilde{\mathbf{C}}_M^{-1} \left(\boldsymbol{m} - \widetilde{\boldsymbol{m}}_i\right) + \mathrm{misfit}_i\right]\right) = \\
&= \frac{1}{c} \exp\left(-\frac{1}{2} \left(\boldsymbol{m} - \widetilde{\boldsymbol{m}}_i\right)^T \tilde{\mathbf{C}}_M^{-1} \left(\boldsymbol{m} - \widetilde{\boldsymbol{m}}_i\right)\right) \exp\left(-\frac{1}{2}\mathrm{misfit}_i\right) .
\end{aligned} \tag{5}$$

The purpose of this transformation is to rewrite PPDF of unknown shape by the misfit and 6-D Gaussian function, which can be integrated later.

The normalizing constant c is obtained by integration over all model parameters and summation over space-time grid points

$$\begin{aligned}
1 &= \sum_i \int \mathrm{PPDF}_i(\boldsymbol{m}) \, \mathrm{d}\boldsymbol{m} \, \Delta V_i = \\
&= \sum_i \int \frac{1}{c} \exp\left(-\frac{1}{2} \left(\boldsymbol{m} - \widetilde{\boldsymbol{m}}_i\right)^T \tilde{\mathbf{C}}_M^{-1} \left(\boldsymbol{m} - \widetilde{\boldsymbol{m}}_i\right)\right) \exp\left(-\frac{1}{2}\mathrm{misfit}_i\right) \mathrm{d}\boldsymbol{m} \, \Delta V_i = \\
&= \sum_i \frac{1}{c} \int \exp\left(-\frac{1}{2} \left(\boldsymbol{m} - \widetilde{\boldsymbol{m}}_i\right)^T \tilde{\mathbf{C}}_M^{-1} \left(\boldsymbol{m} - \widetilde{\boldsymbol{m}}_i\right)\right) \mathrm{d}\boldsymbol{m} \, \exp\left(-\frac{1}{2}\mathrm{misfit}_i\right) \Delta V_i = \\
&= \sum_i \frac{1}{c} \sqrt{(2\pi)^6 \det \mathbf{C}_i^M} \exp\left(-\frac{1}{2}\mathrm{misfit}_i\right) \Delta V_i = \\
&= \sum_i a_i ,
\end{aligned} \tag{6}$$

where we used n-dimensional Gaussian integral and the ΔV_i is a volume belonging to the grid-point i. In our case (uniform sampling in both space and time), it is

$$\Delta V_i = \Delta x \, \Delta y \, \Delta z \, \Delta t , \tag{7}$$

where Δx, Δy, and Δz is grid spacing in direction of the coordinates x, y, and z, respectively, and Δt is time-grid spacing.

We denoted a_i the PPDF integrated over all MT parameters at a given space-time grid point i. It is composed of the analytically estimated uncertainties of all MT parameters (determining the model covariance matrix $\mathbf{C}_i^M$) and misfit of the best model at that grid point

$$a_i = \frac{1}{c} \sqrt{(2\pi)^6 \det \mathbf{C}_i^M} \exp\left(-\frac{1}{2}\mathrm{misfit}_i\right) \Delta V_i . \tag{8}$$

1.1 Marginal probability density

Marginal probability density of the inverted parameters as well as marginal probability densities of some parameters non-linearly related to MT (e.g. strike angle or double-couple percentage, which are not directly inverted, but can be calculated from the inverted moment tensor components) can be determined. To manage this, we generate random samples of MT from a multivariate normal (Gaussian) distribution at each grid point specified by its mean $\widetilde{\mathbf{m}}_i$ and model parameters covariance matrix $\widetilde{\mathbf{C}}_i^M$ (determined in Eqs. 1 and 2). The number of random samples at each grid point i is proportional to a_i, i.e. PPDF integrated over the MT parameters in the specific grid point (Eq. 8). Having an ensemble of random samples drawn from the total PPDF, we can easily plot histograms of parameters of interest (both inverted as well as their combinations) or scattering of nodal planes. Examples are given later.

2 Automated detection of long-period disturbances in seismic records; MouseTrap code

We developed a code `MouseTrap` for automated detection of fling step disturbances in seismic records. The program is available as an ObsPy module under GNU/GPL license at website `http://geo.mff.cuni.cz/~vackar/mouse`. Many of the observed disturbances can be modeled as a seismometer response to an acceleration step on the input [Zahradník and Plešinger, 2005] (Fig. 1). Fitting the synthetic disturbance into real records provides four parameters of the input acceleration step, namely its onset time t_0, amplitude A, azimuth ϕ, and inclination θ. The code can be applied either to an individual record or to a set of records with metadata in a database.

We expect the code to be useful in many applications for automatic data processing, e.g. waveform inversion and S/N ratio evaluation, where detection and removal of contaminated records is a must.

We also developed the code `SwissMouse` for automated analysis of fling step existence in broad-band records of Swiss Digital Seismic Network over the last 18 years, at stations close to located events. Fling steps are present at all types of studied broad-band instruments, at many different stations. We observed a higher percentage of fling steps at some stations. Azimuths of fling steps remain the same at some (but not all) stations. In particular there is a higher occurrence of fling steps with azimuths 30°, 90°, and 150°. Most of the fling steps are horizontal, but a significant number have inclination $\sim 35°$. These preferred directions are very likely related to pendulums in Galperin's design seismometers, so these cases are probably of instrumental origin. There is a good reason (supported by limited authors' experience) to expect, that in instruments operating with pendulums in N, E, Z setup, such as e.g. Guralp CMG 3-T, the disturbances might sometimes be preferentially related to a single component. The fling steps are more common at records with higher PGA and PGV, near the source, and at higher magnitudes (M 1–4 mostly examined). Besides this paper we have also observed such disturbances at short-period instruments, where they are naturally characterized by much shorter durations than at broad-band seismometers.

There are also similar disturbances which can be described as instrument

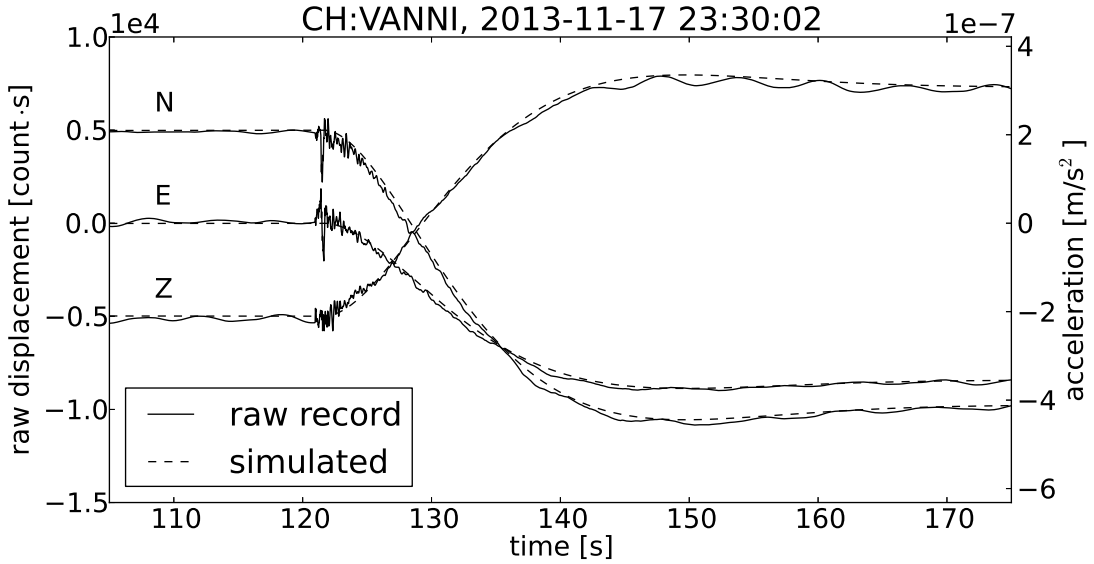

Figure 1: Example of a fling step disturbance in the integrated output (raw displacement) of the Nanometrics Trillium T40 seismometer. The disturbance is well fitted by the simulated instrument response to an acceleration step of amplitude $A = 8.7 \cdot 10^{-7}\,\mathrm{m \cdot s^{-2}}$, azimuth $\phi = 209.7°$, and inclination $\theta = 35.9°$. The recorded earthquake has magnitude $M_{Lh} = 1.7$ (Swiss Seismological Service), its epicentral distance is 1.9 km.

response to a spurious step in the input velocity [Zahradník and Plešinger, 2010], which can be explained as caused by saturation in the force-balance system. These might be implemented in future updates of the `MouseTrap` code, including diagnostics of a joint occurrence of both kinds of disturbances.

3 Covariance matrix of the noise

In this chapter we describe the construction of the data covariance matrix $\mathbf{C}_D$. In our definition, it reflects the properties of the seismic noise. We assume that seismic noise time series can be considered as a stationary Gaussian random process with zero mean. Then the data covariance matrix can be written for a discrete series $x(t_i)$, which represents a single component of seismic noise at a single station, as [Tarantola, 2005, Example 5.1]

$$\mathbf{C}_D = \begin{pmatrix} C(\tau_0) & C(\tau_1) & \cdots & C(\tau_{N-1}) \\ C(\tau_1) & C(\tau_0) & \cdots & C(\tau_{N-2}) \\ \vdots & \vdots & \ddots & \vdots \\ C(\tau_{N-1}) & C(\tau_{N-2}) & \cdots & C(\tau_0) \end{pmatrix} . \tag{9}$$

where $C(\tau_k)$ is a value of covariance function for a time lag τ_k and N is a number of samples in the discrete series $x(t_i)$. For estimation of the covariance function, we assume ergodicity, so that the averaging over realizations can be replaced by averaging over time. Then the covariance for discrete time series may be

estimated as the auto-correlation defined by

$$C(\tau_k) \overset{\text{ergodicity}}{=} (x \star x)[\tau_k] \overset{\text{def}}{=} \frac{1}{2N+1} \sum_{m=-N}^{N} x[\tau_m]\; x[\tau_{m+k}] \; . \tag{10}$$

So far, we have assumed only a single scalar time history of the noise (i.e., a single component of the motion at a single station). Nevertheless, the data covariance matrix could be generalized for the three component noise recordings acquired at L stations. In general, one should assume all potential correlations in the recorded noise wave field, so that the full covariance matrix would consist of 3 times L matrices defined in equation (9). On one hand, since the noise wave field still consists of propagating seismic waves (e.g., surface waves), one cannot neglect the correlation between the components of recorded ground motion at a single station. On the other hand, we assume zero correlations between the noise recordings at different stations. This is valid assumption for stations which are far away from each other and for high frequency seismic noise, so that different noise sources dominate the recording at different stations. For stations close to each other, seismic arrays, collocated sensors, and for low frequency noise, it might be useful to take into account cross-covariance between stations. The data covariance matrix for two stations, each of them with three components (with ordering station first and then components) would be then [Tarantola, 2005, eq. 5.10–5.11]

$$\mathbf{C}_D = \begin{pmatrix} \mathbf{C}_{st1}^{ZZ} & \mathbf{C}_{st1}^{ZN} & \mathbf{C}_{st1}^{ZE} & 0 & 0 & 0 \\ \mathbf{C}_{st1}^{NZ} & \mathbf{C}_{st1}^{NN} & \mathbf{C}_{st1}^{NE} & 0 & 0 & 0 \\ \mathbf{C}_{st1}^{EZ} & \mathbf{C}_{st1}^{EN} & \mathbf{C}_{st1}^{EE} & 0 & 0 & 0 \\ 0 & 0 & 0 & \mathbf{C}_{st2}^{ZZ} & \mathbf{C}_{st2}^{ZN} & \mathbf{C}_{st2}^{ZE} \\ 0 & 0 & 0 & \mathbf{C}_{st2}^{NZ} & \mathbf{C}_{st2}^{NN} & \mathbf{C}_{st2}^{NE} \\ 0 & 0 & 0 & \mathbf{C}_{st2}^{EZ} & \mathbf{C}_{st2}^{EN} & \mathbf{C}_{st2}^{EE} \end{pmatrix} , \tag{11}$$

where blocks on the diagonal (e.g., C_{st1}^{ZZ}, C_{st1}^{NN}, etc.) are given by Eqs. (9 and 10), while at non-diagonal blocks (e.g., C_{st1}^{EN}, C_{st1}^{EZ}, etc.) are given by Eq. (9), except $C(\tau_k)$ is discrete cross-covariance, estimated by discrete cross-correlation, so that, for example,

$$C^{EZ}(\tau_k) \overset{\text{ergodicity}}{=} (x^E \star x^Z)[\tau_k] \overset{\text{def}}{=} \frac{1}{2N+1} \sum_{m=-N}^{N} x^E[\tau_m]\; x^Z[\tau_{m+k}] \; , \tag{12}$$

would be an estimate of cross covariance for East-West ($x^E(t_i)$) and vertical component ($x^Z(t_i)$) noise time series at a single station. The empty blocks are from the assumption that the seismic noise is not correlated between the seismic stations.

We illustrate a data covariance matrix on a simple example in Fig. 2.

3.1 Standardized data calculated using the covariance matrix

The real vs. synthetic waveform match is commonly plotted as it provides visual control of the difference between the reality and a model. For the most simple

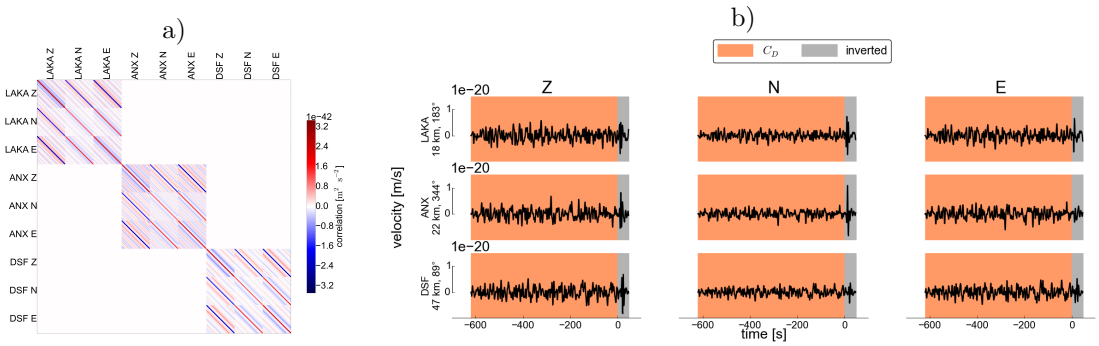

Figure 2: Example of data covariance matrix (panel a) and related seismograms (panel b). We generated synthetic data for three 3-component stations for a given seismic source and added planar wave white noise coming from azimuth 54° and inclination −21°, so all components are affected (panel b). The data covariance matrix $\mathbf{C}_D$ (panel a) is calculated from the before event noise (orange time window in panel b). The data covariance matrix consists of three large non-empty blocks corresponding to three stations, their 3×3 sub-blocks correspond to auto- and cross-covariance of the 3 components. We can see that some components are correlated (red color at the diagonal) and the others anticorrelated (blue color). The correlation between stations is assumed to be zero.

case of the inverse problem with diagonal data covariance matrix with constant data variance σ^2 ($\mathbf{C}_D = \sigma^2\mathbf{I}$), the solution of the inverse problem (eq. 1) is

$$\widetilde{\mathbf{m}} = \left(\mathbf{G}^T \left(\sigma^2\mathbf{I}\right)^{-1} \mathbf{G}\right)^{-1} \mathbf{G}^T \left(\sigma^2\mathbf{I}\right)^{-1} \boldsymbol{d}_{obs} = \left(\mathbf{G}^T\mathbf{G}\right)^{-1} \mathbf{G}^T \boldsymbol{d}_{obs} \ . \tag{13}$$

Then the real/synthetic waveform difference, which is plotted, is also minimized in the L^2-norm. For general $\mathbf{C}_D$ described in this chapter, interpreting such a waveform match as a criterion of the fit quality is problematic, because the misfit value and the difference between the real and synthetic waveform is weighted by the data covariance matrix (Eq. 3). Consequently, a large difference between the observed and simulated waveforms may be caused by frequencies which are actually suppressed in the inversion by the effect of $\mathbf{C}_D$ and the stations with the largest amplitudes might not be the ones with the largest impact. In this section, we present a way how to visualize the waveform difference, which is directly related to the minimized misfit.

Since $\mathbf{C}_D$ is positive-definite matrix by its definition (we use biased estimate of the covariance function in Eqs. 9 and 11), we can use Cholesky decomposition.

$$\mathbf{C}_D^{-1} = \mathbf{L}\mathbf{L}^T \ . \tag{14}$$

Then we can rewrite the misfit definition (Eq. 3) in the following way:

$$\begin{aligned} \text{misfit}_i &= (\boldsymbol{d}_{obs} - \mathbf{G}\widetilde{\boldsymbol{m}}_i)^T \mathbf{L}\mathbf{L}^T (\boldsymbol{d}_{obs} - \mathbf{G}\widetilde{\boldsymbol{m}}_i) = \\ &= \left(\mathbf{L}^T\boldsymbol{d}_{obs} - \mathbf{L}^T\mathbf{G}\widetilde{\boldsymbol{m}}_i\right)^T \left(\mathbf{L}^T\boldsymbol{d}_{obs} - \mathbf{L}^T\mathbf{G}\widetilde{\boldsymbol{m}}_i\right) = \\ &= (\boldsymbol{d}'_{obs} - \boldsymbol{d}'_i)^T (\boldsymbol{d}'_{obs} - \boldsymbol{d}'_i) \ , \end{aligned} \tag{15}$$

where

$$\begin{aligned} \boldsymbol{d}'_{obs} &= \mathbf{L}^T \boldsymbol{d}_{obs} \\ \boldsymbol{d}' &= \mathbf{L}^T \mathbf{G} \widetilde{\boldsymbol{m}}_i \ . \end{aligned} \tag{16}$$

The difference between $\boldsymbol{d}'_{obs}$ and $\boldsymbol{d}'$ (called standardized residuals, according to Dettmer et al. [2014]) is minimized in the L^2-norm, so it can be plotted to visualize waveform agreement as used in inversion. The effect of the automated station weighting and frequency filtering, that are also included in the approach, (shown in Section 5.1) can be seen in $\boldsymbol{d}'_{obs}$ (standardized observed data) and $\boldsymbol{d}'$ (standardized synthetic data) also. As a drawback, the information at components of $\boldsymbol{d}'_{obs}$ (standardized data) may be mixed compared to components of $\boldsymbol{d}_{obs}$ (original data). This may happen if, e.g., the noise on horizontal components E and N is strongly correlated. Then the information about its correlation, contained in $\mathbf{C}_D$, helps in the inverse problem, but the $\mathbf{C}_D$ also causes tradeoff between components E and N of standardized waveforms. This tradeoff is intrinsically connected with removing the effect of the noise correlated between components.

4 Developed method and its technical aspects

The method described in the previous chapters, together with a few other procedures for optimal data selection and some plotting routines, is programmed as a software package ISOLA-ObsPy, which can be used for fully automated moment tensor inversion, including near-real-time data flows, as well as large data sets of previously recorded events.

The package includes automated data retrieval (saved in any file format supported by ObsPy [Krischer et al., 2015] or accessible via ArcLink [*SeisComP3 documentation*]), removal of components with various instrumental disturbances, setting frequency ranges for each station individually according to its distance and event magnitude, and full-waveform inversion in space-time grid around hypocenter. The size of the space-time grid is automatically chosen according to the location uncertainty and magnitude. Time sampling is 100-times higher then the high limit of the inverted frequency band. Spatial sampling can be adjusted by user by entering horizontal and vertical step directly and/or by entering maximal number of grid points.

Grid search over time and space is effectively combined with analytical (least-squares) MT inversion in a Bayesian framework. This way not only the best solution is found, but also the full posterior probability density function of the CMT is inferred. The marginal probability density function for any CMT parameter can be plotted. Data covariance matrix calculated from the before-event noise yields an automated weighting of the stations according to their noise levels and also serves as an automated frequency filter suppressing noisy frequencies. To speed up the inversion, the time demanding tasks such as the Green's function calculations and the spatial grid search are parallelized. The software package is programmed as versatile as possible in order to be applicable in various networks ranging from local to regional.

The code shares some similarities with the broadly used ISOLA software [Sokos and Zahradník, 2013] in terms of the inversion methods and input/output file structures, but most codes have been re-written from the scratch for

maximum computational efficiency (combing Fortran and Python, using ObsPy, NumPy, and MatPlotLib). In contrast to ISOLA, whose advantage is in a friendly manual processing of individual events using Matlab GUI, the new codes are intended rather for a massive automated application on large sets of earthquakes from a database, and/or for near real-time applications.

Although the process is fully automated, the inversion can be visually inspected later. For this reason, many figures are automatically plotted.

The ISOLA-ObsPy software package is available under GNU/GPL licence[1] and can be downloaded from `http://geo.mff.cuni.cz/~vackar/isola-obspy/`, where there is also full documentation.

4.1 Technical solution

Here we add some technical details related to the developed method extending the description in the lead-in of this chapter.

For programming the automated CMT inversion, we have chosen Python because it is powerful and high-level programming language, with a wide range of standard libraries, and it is available for many operating systems. During the development, we appreciated high code readability and syntax which enable to express concepts in a brief way. We wrote the package using object-oriented programming[2]. The core of the package is a class[3] `ISOLA`. This class contains input data (like seismograms and initial location), calculated intermediate products (like the data covariance matrix), and results (e.g. most probable CMT and its uncertainty), as well as methods performing all steps of the calculation. This concept enables an easy implementation of the method to a larger product, like a program for real time data processing or analysis of a large dataset of historical earthquakes.

In the development, we benefit from many standard libraries of Python (e.g. `numpy`, `pyproj.Geod`, `psycopg2`, `matplotlib`, etc.) and seismological toolbox `ObsPy`.

The calculation of Green's functions is out of scope of the thesis. They are computed by code `axitra` [Bouchon, 1981; Coutant, 1989], which is called from our code.

The most computationally demanding parts of the calculation are calculation of the Green's function and searching the solution of the inverse problem on space-time grid. These two parts are parallelized using Python module `multiprocessing`. This module runs separate tasks as subprocesses and allows the programmer to fully leverage multiple processors on a given machine.

[1] The GNU General Public License (GNU GPL) is a widely used free software license, which guarantees end users the freedom to run, study, share and modify the software. Available at `https://gnu.org/licenses/gpl.html`

[2] concept of programming, which uses "objects", which may contain several data fields (often called 'attributes') and code in the form of procedures (called 'methods')

[3] program-code-template for creating objects, providing initial values for member variables and implementations of the methods

4.2 Results plotting

The method is optimized for automated data processing, but a possibility for later visual inspection of algorithm is highly desirable in many applications. For that reason, the code has procedures for plotting various figures visualizing input data, result stability, uncertainty, waveform fit, as well as some intermediate products, like the figure of the covariance matrix. Here we show just one example of them, a figure showing spatial stability of the solution (Fig. 3).

In addition to these figures, the ISOLA-ObsPy package contains a function for creating an HTML page containing a description of the result illustrated these figures. We can decide which plots should be included in HTML report and/or add a reference solution for comparison by setting parameters of the function.

Beside graphical output, the code provide also a plain text output of moment tensor itself, its position, and its tensor decomposition.

5 Tests and applications of the developed method

5.1 Synthetic tests

There are three representative synthetic tests presented in this section. They show that the proposed method can not only assess the uncertainty of the CMT solutions with respect to seismic noise, but it can also improve the CMT results. The improvement is possible because when analyzing the noise, the inversion can automatically be focused onto the least noisy part of the data.

5.1.1 Dependence of the uncertainty on the noise level and number of stations

To illustrate the performance of the proposed method, we conduct a synthetic test showing behavior of the Bayesian inversion for different noise levels and station configurations (Fig. 4). We generated synthetic waveforms (in the same velocity model as used in the inversion), then we added white noise of specified level, and used it as "data" in the inversion. Narrowing the marginal probability of each parameter can be observed for higher number of stations, lower noise level, and better azimuthal coverage. The marginal probability densities are plotted by method described in Section 1.1. The dependence on the noise level is driven by the data covariance matrix $\mathbf{C}_D$ (described in Chapter 3), which reflects the properties of before-event noise.

The marginal probability distribution is not always centered at the true solution (for which synthetic seismograms were generated; red line in the figure), but usually close to the best fitting model, which can be biased. The bias changes for every realization of random white noise. The 'DC %' parameter never has a maximum at 100 % because every perturbation around a pure-DC mechanism results in a non-DC part, so obtaining pure-DC moment tensor is highly improbable when generating realizations within a given probability density function. But maximum probability of 'DC %' gets closer to original 100 % when the uncertainty is decreasing.

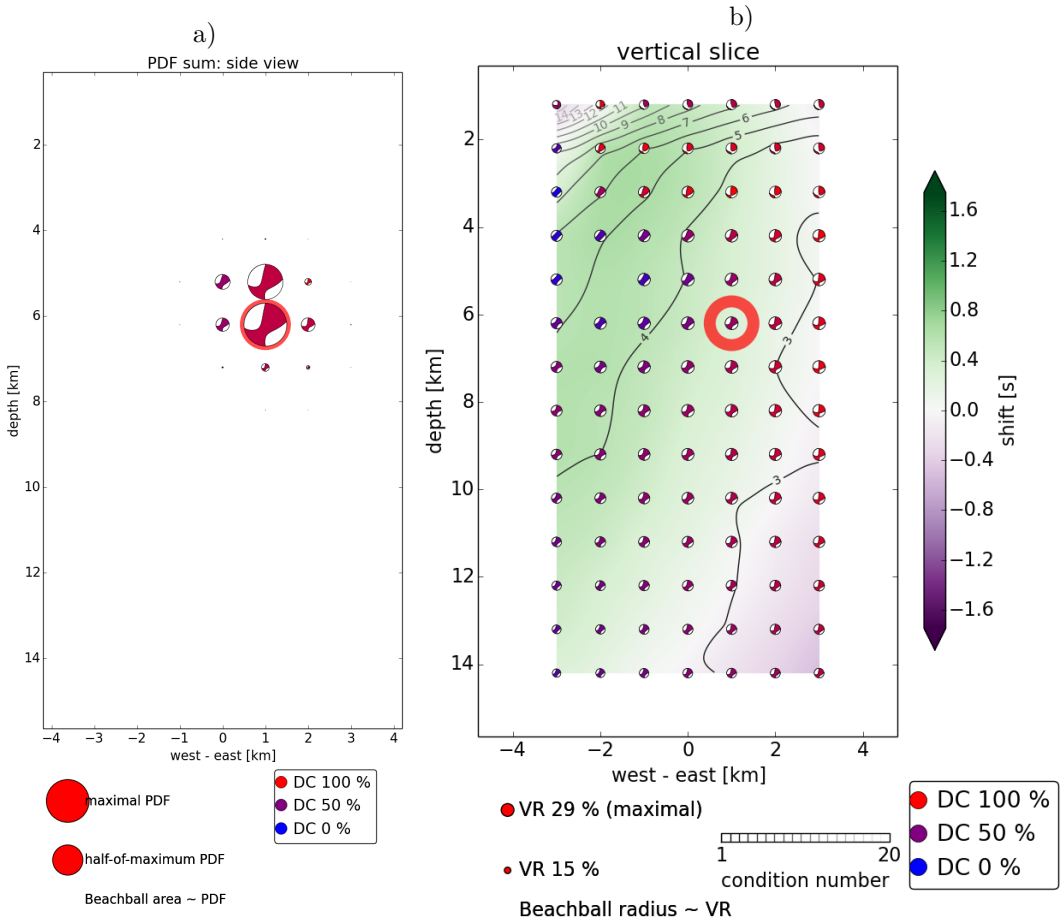

Figure 3: Solution varying with depth and west-east coordinate (view from the south). The color of the beachball corresponds to the DC percentage for the best solution at a given grid point. In panel (a), the size of the beachballs corresponds to the posterior probability density function (PPDF) and the PPDF is summed over third dimension (N-S coordinate) and time. In panel (b), the beachball size corresponds to the variance reduction (VR), the solutions are shown in the plane in which the best solution (circled) lies, the color in the background corresponds to the inverted centroid time at a given grid point, and the contour lines show the condition number. Plotted for an $M_W = 3.7$ earthquake at Sargans, Switzerland on 2013-12-27 07:08:28.

number of station	3	8	3	3	8
noise	strong	strong	weak	weak	weak
max. azimuthal gap	138° (good)	105° (good)	329° (poor)	138° (good)	105° (good)
condition number	5	6	10	5	6
variance reduction	14 %	8 %	71 %	71 %	62 %

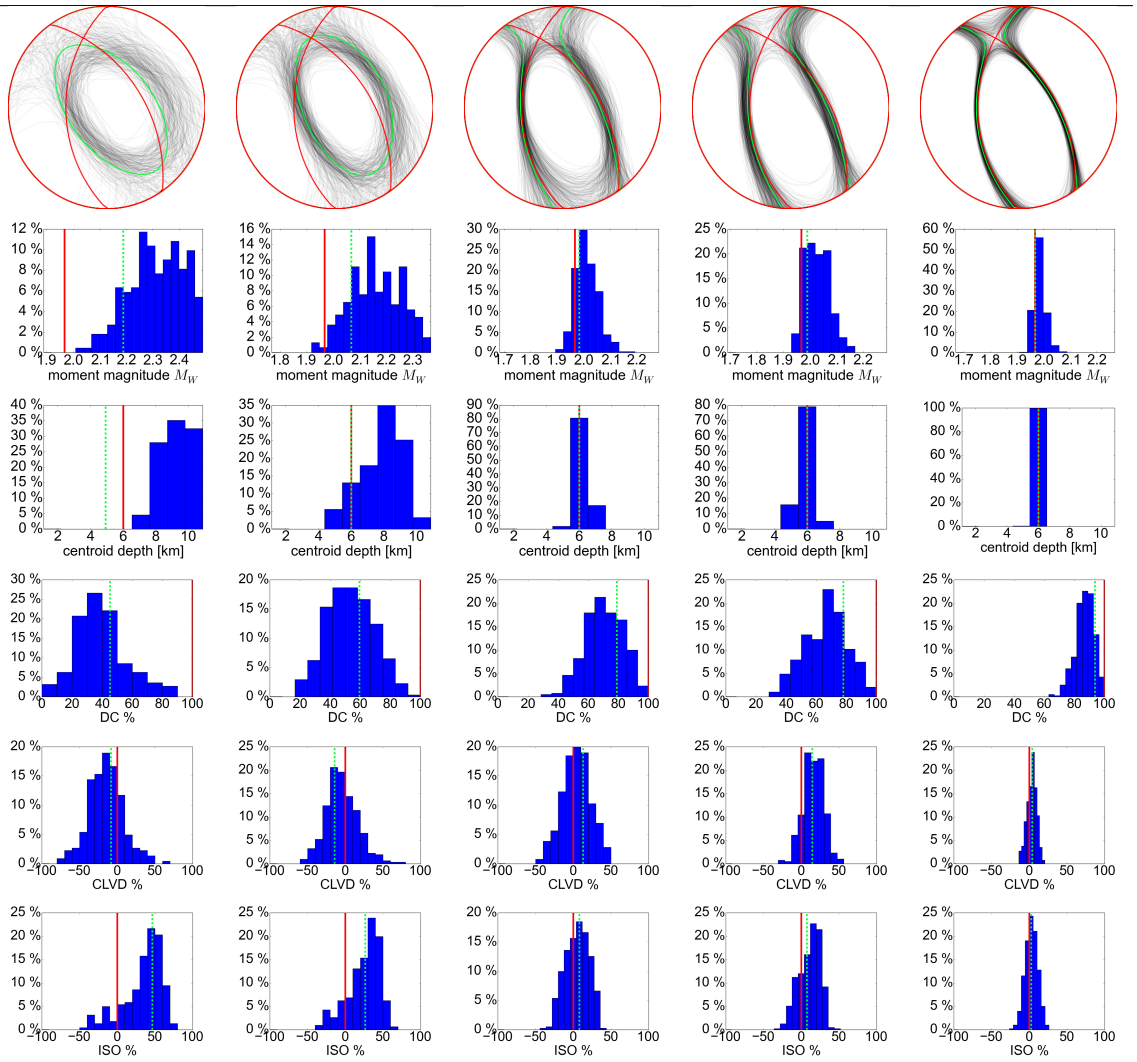

Figure 4: Case example (synthetic test), how the Bayesian uncertainty of the resulting CMT varies in five different configurations. 400 focal mechanisms were generated randomly based on the calculated PPDF (see Section 1.1). The configurations differ by the number of the stations, their azimuthal distribution, and by the noise level. True parameters are shown in red and the best solution by the green dotted line. Marginal probability densities are shown for nodal lines, moment magnitude Mw, centroid depth and for the MT decomposed into its double-couple, CLVD and isotropic component [Vavryčuk, 2015]. The marginal probability function gets narrower (more focused) as the number of the stations increases, their azimuthal coverage improves, and as the noise decreases. Noise denoted 'strong' has 4 times higher standard deviation than 'weak' one.

5.1.2 White noise test, station dependent

In practice, the seismic noise level often varies from station to station. An automatic algorithm or manual operator needs to choose the stations according their signal-to-noise ratio. In this test we examine ability of the data covariance matrix to automate such a procedure, i.e. to prefer the stations at which the noise level is low. Because in practice we often use the same frequency range at many stations, and this range is relatively narrow (1–2 octaves wide), for simplicity here we assume a white noise.

We simulated waveforms of an event with a given focal mechanism, adding a strong white noise to 3 stations of 5, and weak noise to the others. The level of the "strong noise" was chosen to be such that in manual processing such stations would be eliminated. The reason was to test the capability of the procedure to manage extreme conditions. Then we sampled down the waveforms to the rate 1.2 Hz, dropping frequencies above the Nyquist frequency, and then we filtered them by Butterworth filter to frequency range 0.02–0.15 Hz.

The results are presented in Fig. 5. As a reference, we show best-fitting solution with a diagonal $\mathbf{C}_D$ (the same standard deviation for all stations). It is given just as an example of a common approach for the purpose of comparison with our new method. The covariance matrix automatically down-weighted the strongly disturbed stations, so that the inversion is controlled almost entirely by the low-noise stations. It usually improves results, but sometimes might produce unfavorable station geometry. To identify such cases, we recommend to have a look at the plot of standardized data together with the plot of the station geometry (panels (a) and (g) in Fig. 5).

5.1.3 Colored (correlated) noise

In real data we always encounter a frequency-dependent noise, and standard manual CMT inversions need to carefully select a frequency range with suitable signal-to-noise ratio. For example, in regional CMT inversions, we can usually use only frequency range below the microseism noise. In this synthetic test we study whether the covariance matrix of the data is able to avoid the noisy part of spectrum automatically.

We simulated waveform for the same focal mechanism as in the previous example and added coloured noise of the same spectral content to all stations. The noise is strong between frequencies 0.05–0.25 Hz, while it is negligible outside this frequency band. Again, the level of the strong noise is such that in manual processing that spectral range would be avoided. Then we down-sampled the waveforms to the rate 4 Hz, dropping frequencies above the Nyquist frequency, and then we filtered them by Butterworth filter between 0.10–0.50 Hz.

The results are shown in Fig. 6. It shows that the new method with the data covariance matrix avoids using the noisy frequency range itself, so it indeed works as an automated filtering scheme.

In both synthetic tests we compare the new method (which uses the full data covariance matrix $\mathbf{C}_D$, described in Chapter 3) with solution using diagonal $\mathbf{C}_D$, which assumes the same standard deviation for all stations. The method with diagonal $\mathbf{C}_D$ is equivalent to simple minimization of difference between the observed and simulated data in L^2 norm, which is common in MT inversion.

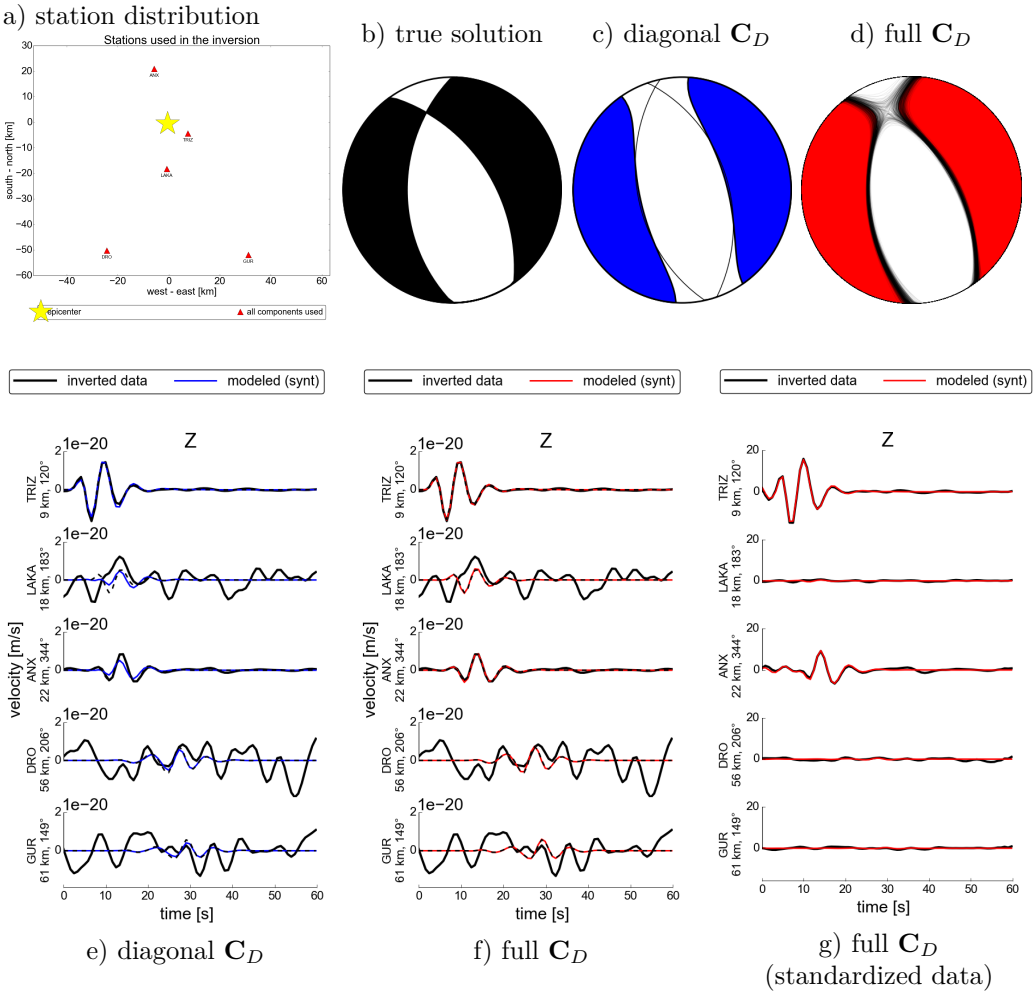

Figure 5: White noise synthetic test: (a) source-station configuration, (b) mechanism for which waveforms were generated ('true solution'), (c) best-fitting solution with a diagonal $\mathbf{C}_D$ (the same standard deviation for all stations), (d) best-fitting solution with full (i.e. block-diagonal) data covariance matrix $\mathbf{C}_D$ (Chapter 3). Waveform comparison for: (e) solution with a diagonal $\mathbf{C}_D$, (f) solutions with full $\mathbf{C}_D$–original seismograms and (g) solutions with full $\mathbf{C}_D$–multiplied by Cholesky decomposition of the $\mathbf{C}_D$ (see Section 3.1), 'standardized data'. Panels (e–g) show original waveforms without noise (dashed black lines), waveforms with the added white noise which were inverted (solid black lines), and modeled waveforms for the retrieved focal mechanism (colored solid line). Comparing panels (f) and (g) it is demonstrated that the covariance matrix strongly up-weighted the weak-noise stations.

In this sense, the new method represents improvement compared to the common approach. We observe that the new method finds the best solution closer (both in time and space) to the 'right' centroid position than the method with a diagonal $\mathbf{C}_D$.

5.2 Inversion of real events — Comparison with Swiss MT catalog

In order to evaluate the performance of the proposed algorithm, we systematically compare CMT solutions using this approach with an independent methodology. As a reference event data set we have selected all (139) events with magnitude ≥ 3 from the Swiss earthquake catalogue from 1999 to June 2015. We compare the results from our method with moment tensor solutions obtained from the scmtv module from SeisComP3 package (hereafter called as 'manual processing'). For both methods, a similar set of 1-D Green's Functions, optimized for the Alpine region [Diehl et al., 2009], is used. Local and Regional MT catalogues for Switzerland have been produced by the SED in the past [Bernardi et al., 2004; Braunmiller et al., 2002], though at the SED these methods have been discontinued and now are replaced by the scmtv approach. For both the methods, all broadband data that is available in the archives of the SED are used. Sensors used in the inversion are restricted to broadband sensors ranging from 40s–120s, though the majority of 120s.

The manual processing uses the workflow implemented within the routine catalogue curation at the Swiss Seismological service. The methodology is based on the linear least squares inversion of Dreger [2003]. The methodology assumes that the isotropic component is zero, the epicentral coordinates are fixed (though the depth can vary), and the source time function is fixed, so it is an MT rather than CMT approach. A limited set of predefined parameters is used to select stations and prepare the data, which is automatically implemented depending on the events' Local Magnitude (ML) as contained in the earthquake catalogue. An automatic algorithm can be applied to select the optimal set of stations and event depth that produces the best MT, taking into account the Variance Reduction and the % Double Couple of the solution, whilst retaining as many stations as possible. Interactively, the solution can be tweaked to select and remove individual station components.

Of the 139 candidate events, MT solutions were obtained for 40 events. The remaining events could not provide a high quality solution for various reasons: too few station components provide high waveform fits with high Variance Reduction due to high background noise, too few stations are available (a small event is located at edges of the network, or the event occurred during the start of the network when station density was sparse). These 40 events were also processed by our new automated code.

The automated procedure followed using the proposed algorithm; all broadband stations within a radius controlled by the M_L magnitude (obtained during catalogue creation at the Swiss Seismological Service) were used. The maximum epicentral distance was limited according to ad hoc formula $r < 2^{2 \cdot M_L}$ km. Moreover, stations closer than 2 km were removed, because they make inversion unstable in many cases. Stations components, where instrumental disturbances

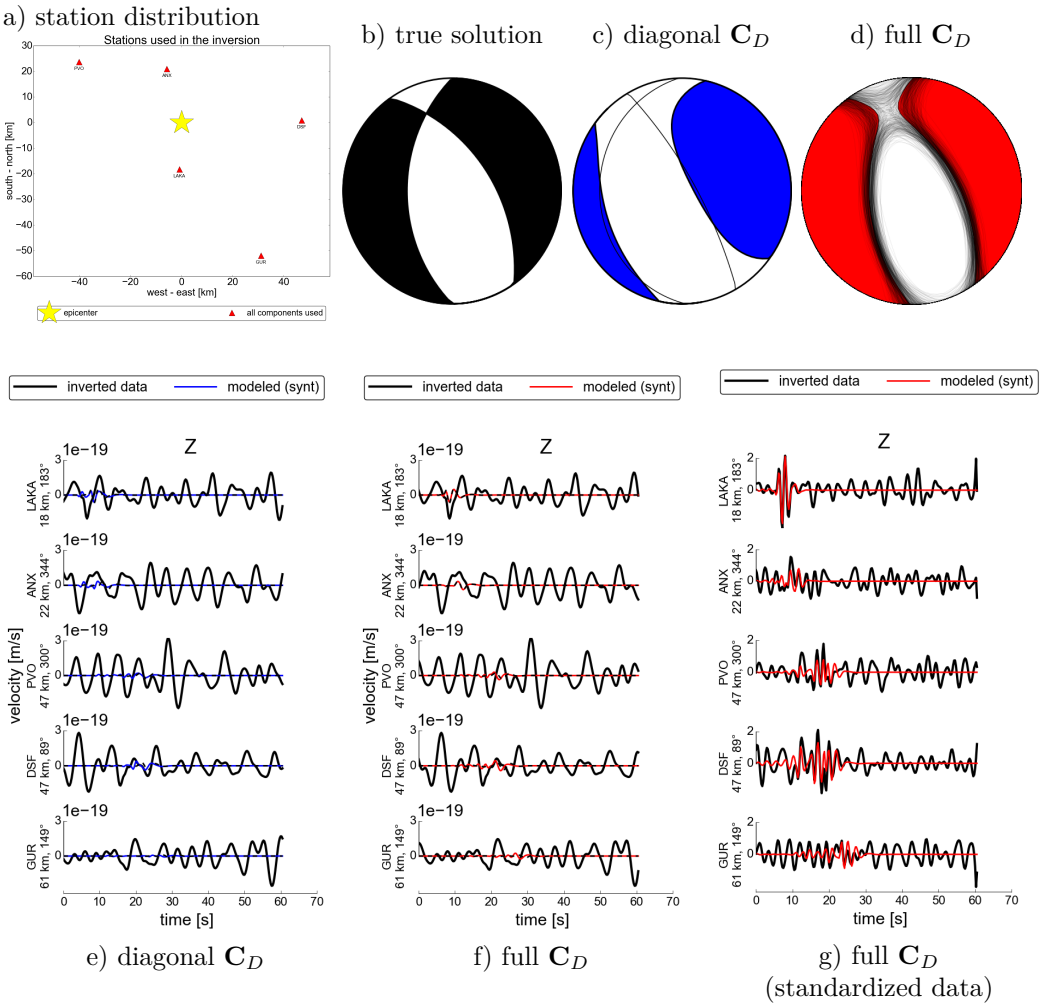

Figure 6: Same as Fig. 5, but for colored noise synthetic test: Strong noise in the frequency band 0.05–0.25 Hz at all stations. The inverted frequency band is 0.10–0.50 Hz, so only its higher part is not disturbed (noise free). The inversion with the covariance matrix $\mathbf{C}_D$ (panel d) provides a solution close to the right one, contrasting with a wrong solution with a diagonal $\mathbf{C}_D$ (panel c). Comparing panels (f) and (g) it is obvious that the covariance matrix serves as an automatic frequency filter enhancing the undisturbed part of the spectrum, thus improving the inversion.

were detected automatically by the MouseTrap code [Vackář et al., 2015], were removed. Also eliminated were records with data gaps in the period required for the earthquake and the noise analyses. The code does not remove any station with high noise because we wanted to test practical ability of the covariance matrix to manage datasets with noisy stations. We require at least 2 stations which have at least 5 usable components, otherwise the event was removed.

Prior to the inversion, the mean was subtracted from the records and 4-pole Butterworth bandpass filter was applied restricting the frequency range to 0.02–0.15 Hz. Moreover, for stations with epicentral distance larger than 100 km, the high frequency limit was restricted in such a way that the minimum wavelength is no more than 5 times shorter than the source to station distance for a reference S-wave velocity 3 km/s. The restriction is to prevent errors arising from inaccurate Earth model resulting in Green's function modeling errors [Hallo and Gallovič, 2016] as well as limited frequency range of the sensor. The centroid position was searched on a grid with sampling 1 km (both in horizontal and vertical direction).

Comparison of the automatic and manual processing is illustrated in Fig. 7. The comparison is quantified by measuring the difference in the orientation of the DC parts of the moment tensors using Kagan's angle, and the difference in depth and moment magnitude M_W. The majority of the automatically processed events (over 70 %) have similar focal mechanism as that obtained in the manual SeisComP3 processing, as expressed by their Kagan angle 0°–20°. Events with large Kagan angle were inspected manually; in all cases, there was another problem with the event, e.g. large azimuthal gap, a not-detected disturbance in inverted waveforms, unstable mechanism strongly varying with depth with almost the same variance reduction, or a combination of these problems. The difference in moment magnitude is below 0.05 at the majority of the events, and within 0.15 in more than 90 % cases. We also compared the inverted centroid depth, and found the difference lower than 2.5 km for 44 % of the events. Taking into account that the station set was usually different in both methods we consider these results as a good agreement.

In addition to this comparison we also summarize our new automatic solutions for all 139 inverted events of Swiss Digital Seismic Network including also events having no counterpart in the manual processing. At each inverse problem we have to decide whether we trust the solution or not. Although some objective measures, like variance reduction or condition number, might be helpful in this point, the decision is always partly subjective and depends on specific application. For the described procedure, we empirically set up a criterion which defines reliable ("trusted") solutions based on variance reduction VR, condition number CN (square root of the ratio of the maximal to the minimal eigenvalue of the matrix $\mathbf{G}_i^T\mathbf{C}_D^{-1}\mathbf{G}_i$ in Eq. 1), double-couple percentage DC, and standard deviation of the following parameters: double-couple and CLVD percentage, moment magnitude M_w, centroid time t, and centroid position x, y, z. The standard deviation of parameters is measured from the points sampling the calculated PPDF. The criterion to consider the solution as reliable is

$$VR > 0.5 \ \wedge \ CN < 8 \ \wedge \ DC > 50\,\% \ \wedge \\ \wedge \ \frac{\sigma_{DC} + \sigma_{CLVD}}{100\,\%} + \frac{\sigma_{M_w}}{1} + \frac{\sigma_t}{1\ \mathrm{s}} + \frac{\sigma_x + \sigma_y + \sigma_z}{1\ \mathrm{km}} < 2\ . \tag{17}$$

The formula indicates trust in solutions with good waveform fit, which are well

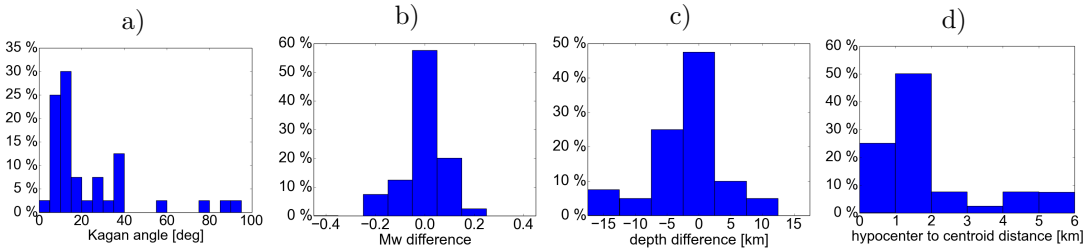

Figure 7: Statistics of the comparison between the new automatic processing of 36 earthquakes recorded in Swiss Digital Seismic Network and their manual processing in scmtv module of SeisComP3. Similarity of the solutions is expressed by (a) Kagan's angles, (b) differences in moment magnitude, and (c) differences in centroid depth, and (d) centroid position. All the events are shallow earthquakes with hypocenter depth up to 35 km, magnitudes are between 3.0–5.0.

resolved (measured by the condition number), with dominant DC part (assuming tectonic origin), and with small uncertainty. The variance reduction is calculated using the standardized data ($\boldsymbol{d}'_{obs}$ and $\boldsymbol{d}'$, Section 3.1).

From the 139 events there were 24 events skipped, because too few stations were available. Of the 115 remaining events, there were 45 events which passed the criterion (Eq. 17). These events, together with their solutions, are plotted in Fig. 8 and the statistic of some of their parameters is plotted in Fig. 9. Most of the trusted events have their variance reduction in the range 0.8-0.9 and condition number between 2–4. From this set, 32 events have their counterpart in the manual processing and 13 events were newly obtained. The 70 untrusted events include also 8 events previously manually processed. We inspected in detail all the removed and newly added events one by one. In case of 8 untrusted events, in most cases we consider that our result is not really reliable. This does not necessary mean that the result from the manual processing is not reliable too, the proper selection of stations and components as well as some other operations in manual processing may help in these specific cases. Inspecting visually all 13 newly obtained events, we confirmed all. We speculate that the reason why manual solutions cannot be made is because of the inflexibility of the manual method to accommodate narrow bandpasses in noisy records, which is a key feature of the proposed method.

A list of all results linked with detailed output for each event is available at `http://geo.mff.cuni.cz/~vackar/CH_catalog/`. For each event, it includes several automatically generated plots and tables in form of a HTML page: centroid location, moment tensor and its decomposition including uncertainty visualization, quality measure VR and CN, uncertainty histogram for several parameters, list and map of used station, waveform fit, noise, and spectral plots, data covariance matrix plot, and figures of the grid of solutions showing posterior probability density function, centroid time, variance reduction, condition number and the best solution at each grid point.

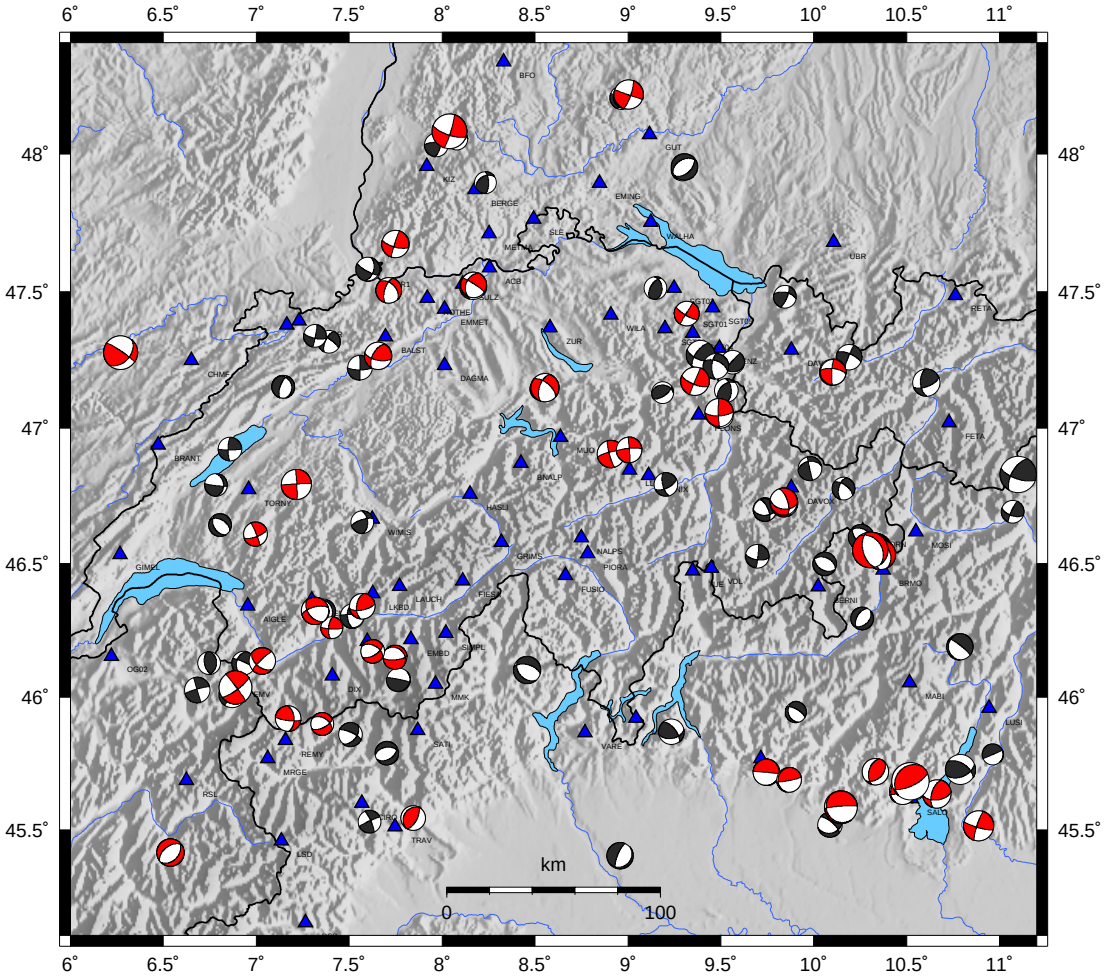

Figure 8: Map of all events with a CMT solution calculated by the proposed method. Events which passed the criterion (Eq. 17), i.e. "trusted events", are shown in red, the others in black. The stations available from the SED data archives at arclink.ethz.ch are shown by blue triangles. Note that only a specific subset of the stations was used in the inversion of each MT. Magnitudes are between 3.0–5.0, hypocenter depths are up to 35 km.

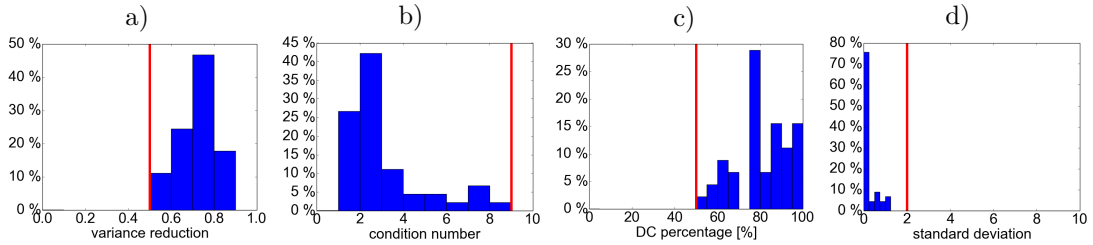

Figure 9: Statistics of quality measures for 45 earthauakes of Swiss earthquake catalogue whose focal mechanisms were newly obtained by the automatic processing and evaluated as reliable by the automated criterion (Eq. 17). Note reasonable reliability of the new solutions, expressed by their (a) high values of the variance reduction, (b) low condition number, (c) low DC percentage, and (d) low combined standard deviation of CMT parameters (see Eq. 17). The cut-of value of the criterion is shown by the red line.

Conclusion and perspectives

The thesis is focused on development of a new, fully automated method for a centroid moment tensor (CMT) inversion. This task covers a wide range of topics, e.g. data selection and retrieval, disturbance detection, seismogram preparation and filtration, station weighting, solution of the inverse problem, uncertainty assessment, result plotting and output presentation etc.

In the beginning of the PhD work, we dealt with a closely related topic, a velocity model, which is a prerequisite for the CMT inversion [Vackář et al., 2014]. We studied how an existing model can be improved to explain the observed seismic waves including leaking modes. Than we focused on the main theme, with a special focus on data quality control, disturbance detection, and uncertainty assessment [Vackář et al., 2015, 2017]. We accented this topic because we wanted to have a robust method with reliable outputs. Therefore, the main results of the work are three papers [Vackář et al., 2014, 2015, 2017], a code for automated CMT inversion freely available at `http://geo.mff.cuni.cz/~vackar/isola-obspy/`, and the thesis.

Our newly developed method and code for the CMT inversion is innovative in the following aspects: (i) the CMT inversion is fully automated, no user interaction is required, although the details of the process can be visually inspected later, using many figures which are automatically plotted. (ii) The automated process includes detection of disturbances. The detection, although not including all types of disturbances, and further development is welcome, avoids most of problems which can cause misleading results. (iii) The data covariance matrix calculated from before-event noise is used. It works as an automated frequency filter and station weighting according to the noise level. (iv) Bayesian approach is used, so not only the best solution is obtained, but also the posterior probability density function. (v) A space-time grid search effectively combined with the least-squares inversion of moment tensor components speeds up the inversion and allows to visually inspect solution variability over the grid.

Some of these features were used by other authors, but the combination of them is novel. To the best of our knowledge, automated MT solution using a Bayesian approach was published just by Stähler and Sigloch [2014] for teleseismic events. The combination of an analytical solution for the MT components with a spatial-temporal grid-searching was suggested by the same authors, but we do not know any other study using it in practice. We did not find also any other Bayesian method eliminating disturbances in seismograms, although hierarchical weights [Dettmer et al., 2014] could overcome this issue. Other works using Bayesian inversion of MT or CMT, which are not automated, include Duputel et al. [2012], Mustać and Tkalčić [2016], and Wéber [2006]. We differ not only in automation and analytical determination of MT components, but also in construction of the data covariance matrix using a non-parametric approach.

We have demonstrated usefulness of the data covariance matrix in terms of automatically identifying a set of stations and frequency ranges most suitable for the waveform inversion. In this sense, our new method is more efficient than various existing procedures in which the inversion is repeatedly performed in different frequency ranges, either manually, or automatically. Our proposed approach seems to be useful for weak events and records with low signal-to-noise ratio, where the

seismic noise is a dominant source of errors. It is important to keep in mind, that such uncertainties correspond just to noise in data, and do not reflect the errors in Green's functions or any other sources of errors. So the obtained uncertainties are usually underestimated in real cases. For more general use, it would be useful to combine our approach (covariance matrix from before-event noise covariance) with some other methods reflecting Green's function uncertainty.

The automated procedure has been tested by comparison with manually processed moment tensors of all events greater than M≥3 in the Swiss catalogue over 16 years using data available at the Swiss data center at arclink.ethz.ch. The quality of the results of the presented automated process is comparable with careful manual processing of data.

The method, developed in the thesis, is programmed in Python and our code is freely available. For its applicability to wider range of seismic events and to make it more user-friendly, some extensions and new features, which were out of scope of the thesis, are welcomed. This further development does not need to be done by the author himself only, but can be done be other developers. The code is open source, so anyone can download the source code and modify it, and also to suggest to incorporate his modified version to the original one. The development is welcomed especially in the following areas: reflecting Green's function uncertainty in the covariance matrix [Bodin et al., 2012; Dettmer et al., 2012; Hallo and Gallovič, 2016], multi-point source approximation [Zahradník and Sokos, in press], detection of other types of disturbances as well as detection of clipped records, and using other codes than Axitra for calculation of Green's functions.

References

Bernardi, F., J. Braunmiller, U. Kradolfer, and D. Giardini (2004). Automatic regional moment tensor inversion in the European-Mediterranean region. *Geophys. J. Int.* **157** (2), 703–716.

Bodin, T., M. Sambridge, H. Tkalčić, P. Arroucau, K. Gallagher, and N. Rawlinson (2012). Transdimensional inversion of receiver functions and surface wave dispersion. *J. Geophys. Res. Solid Earth* **117** (B2).

Bouchon, M. (1981). A simple method to calculate Green's function for elastic layered media. *Bull. Seism. Soc. Am.* **64** (1), 93–107.

Braunmiller, J., U. Kradolfer, M. Baer, and D. Giardini (2002). Regional moment tensor determination in the European-Mediterranean area – initial results. *Tectonophysics* **356**, 5–22.

Coutant, O. (1989). Program of numerical simulation AXITRA. *Res. Rep. LGIT (in French), Universite Joseph Fourier, Grenoble.*

Dettmer, J., S. Molnar, G. Steininger, S. Dosso, and J. Cassidy (2012). Trans-dimensional inversion of microtremor array dispersion data with hierarchical autoregressive error models. *Geophys. J. Int.* **188** (2), 719–734.

Dettmer, J., R. Benavente, P. R. Cummins, and M. Sambridge (2014). Trans-dimensional finite-fault inversion. *Geophys. J. Int.* **199** (2), 735–751.

Diehl, T., E. Kissling, S. Husen, and F. Aldersons (2009). Consistent phase picking for regional tomography models: application to the greater Alpine region. *Geophys. J. Int.* **176**, 542–554.

Dreger, D. S. (2003). TDMT_INV: Time domain seismic moment tensor inversion. In: *International Geophysics*. Vol. 81. Elsevier, 1627.

Duputel, Z., L. Rivera, Y. Fukahata, and H. Kanamori (2012). Uncertainty estimations for seismic source inversions. *Geophys. J. Int.* **190** (2), 1243–1256.

Hallo, M. and F. Gallovič (2016). Fast and cheap approximation of Green function uncertainty for waveform-based earthquake source inversions. *Geophys. J. Int.* **207** (2), 1012–1029.

Krischer, L., T. Megies, R. Barsch, M. Beyreuther, T. Lecocq, C. Caudron, and J. Wassermann (2015). ObsPy: a bridge for seismology into the scientific Python ecosystem. *Computational Science and Discovery* **8** (1).

Mustać, M. and H. Tkalčić (2016). Point source moment tensor inversion through a Bayesian hierarchical model. *Geophys. J. Int.* **204** (1), 311–323.

Sambridge, M. (2014). A Parallel Tempering algorithm for probabilistic sampling and multimodal optimization. *Geophys. J. Int.* **196**, 357–374.

Sambridge, M. and K. Mosegaard (2002). Monte Carlo methods in geophysical inverse problems. *Rev. Geophys.* **40** (3), 1009.

SeisComP3.org. SeisComP3 documentation. url: `https://www.seiscomp3.org/wiki/doc/applications/arclink` (visited on 01/24/2017).

Sokos, E. and J. Zahradník (2013). Evaluating centroid-moment-tensor uncertainty in the new version of ISOLA software. *Seismol. Res. Lett.* **84**, 656–665.

Stähler, S. and K. Sigloch (2014). Fully probabilistic seismic source inversion-Part 1: Efficient parameterisation. *Solid Earth* **5** (2), 1055–1069.

Tarantola, A. (2005). Inverse problem theory and methods for model parameter estimation. siam.

Vackář, J., J. Zahradník, and E. Sokos (2014). Strong fast long-period waves in the Efpalio 2010 earthquake records: explanation in terms of leaking modes. *J. Seismolog.* **18**, 81–91.

Vackář, J., J. Burjánek, and J. Zahradník (2015). Automated detection of long-period disturbances in seismic records; MouseTrap code. *Seismol. Res. Lett.* **86**, 442–450.

Vackář, J., J. Burjánek, F. Gallovič, J. Zahradník, and J. Clinton (2017). Bayesian ISOLA: new tool for automated centroid moment tensor inversion. *Geophys. J. Int.* **210** (2), 693–705.

Vavryčuk, V. (2015). Moment tensor decompositions revisited. *J. Seismolog.* **19** (1), 231–252.

Wéber, Z. (2006). Probabilistic local waveform inversion for moment tensor and hypocentral location. *Geophys. J. Int.* **165** (2), 607–621.

Zahradník, J. and A. Plešinger (2005). Long-period pulses in broadband records of near earthquakes. *Bull. Seism. Soc. Am.* **95**, 1928–1939.

Zahradník, J. and A. Plešinger (2010). Toward understanding subtle instrumentation effects associated with weak seismic events in the near field. *Bull. Seism. Soc. Am.* **100**, 59–73.

Zahradník, J. and E. Sokos (in press). ISOLA code for multiple-point source modeling. In: *Moment Tensor Solutions—A Useful Tool for Seismotectonics*. Ed. by S. D'Amico. Springer. url: `http://geo.mff.cuni.cz/~jz/papers/ISOLA_bookchapter.pdf`.

Author's publications

Related with the thesis topic

J. Vackář, J. Zahradník, and E. Sokos [2014]. Strong fast long-period waves in the Efpalio 2010 earthquake records: explanation in terms of leaking modes. *J. Seismolog.* **18**, 81–91

J. Vackář, J. Burjánek, and J. Zahradník [2015]. Automated detection of long-period disturbances in seismic records; MouseTrap code. *Seismol. Res. Lett.* **86**, 442–450

J. Vackář, J. Burjánek, F. Gallovič, J. Zahradník, and J. Clinton [2017]. Bayesian ISOLA: new tool for automated centroid moment tensor inversion. *Geophys. J. Int.* **210** [2], 693–705

Non-related with the thesis topic

O. Novotný, J. Vackář, and E. Sokos [2015]. Dispersion of Love waves from the 2010 Efpalio earthquake in the Corinth Gulf region, Greece. *J. Seismolog.* **19**, 801–806

J. Málek, J. Brokešová, and J. Vackář [2017]. Mid-European seismic attenuation anomaly. *Tectonophysics* **712**, 557–577